IEEE Access
Multidisciplinary | Rapid Review | Open Access Journal

Received 13 April 2022, accepted 29 June 2022, date of publication 7 July 2022, date of current version 18 July 2022.

Digital Object Identifier 10.1109/ACCESS.2022.3189022

RESEARCH ARTICLE

Multiprobe Radiation Simulation Method for Phased Array Radar Performance Evaluation

RUOXI XU[1], XIAO HE[1], YUANYUAN YANG[1], HONGDA YAO[1], AND QIAN WU[2]
[1]Beijing Institute of Control and Electronic Technology, Beijing 100038, China
[2]Beijing Institute of Control Engineering, Beijing 100190, China

Corresponding author: Ruoxi Xu (xurxbeijing@163.com)

ABSTRACT The phased array radar exhibits improved tracking accuracy and anti-jamming performance with multi-beam tracking, beam agility, and adaptive beam-forming capabilities. The performance evaluation of the phased array radar is essential for the product designing and development stage. However, the conventional injection simulation and triad radiation simulation methods are not suitable for phased array radars. Therefore, new methods for radiation simulation are required on an urgent basis for the performance evaluation of phased array radars in a reliable, reliable, and repeatable way. This paper focuses on designing a practical anechoic chamber system of multi-probe radiation suitable for phased array radars. The appropriate test distance, the physical size of the anechoic chamber, the multi-probe radiation signal model, and the number of probes required were discussed. Furthermore, an inversion method based on least squares was proposed to solve the complex weights of the probes, thereby simulating the desired apparent center position. The simulation results demonstrated the effectiveness of the proposed method.

INDEX TERMS Anechoic chamber, apparent center position, multi-probe radiation, phased array radar.

I. INTRODUCTION

Radar is the core component of a guidance system, which quickly and accurately identifies, locates, and tracks targets through searching, tracking, and imaging [1], [2]. Modern radars have incorporated many new technologies, such as the phased array radar technology, multi-beam tracking technology, and high-resolution forward-looking imaging technology, to adapt to complex natural backgrounds and environments with strong electromagnetic interference and improve target adaptability and detectability [3]–[5].

In recent years, phased array technology has been widely used. The standard active phased array radar generally consists of multiple subarrays; the front end of each subarray connects with the multiple transmit/receive (T/R) modules and antennas, while the back end connects with the baseband signal processing module. Therefore, the active phased array radar carries out analog and digital phase modulation functions, which can realize a rapid change in transmitting and receiving beams. Moreover, it exhibits broadband signal receiving capacity, rapidly processing the received echo and interference signals. Digital beam-forming, simultaneous multi-target tracking, and adaptive nulling based on the subarray-level active phased array radar are promising technologies that could considerably improve the tracking accuracy and anti-jamming performance of the radar system [6]–[9].

A definite challenge in the radar design process is the testing and verification of its performance and resistance to natural backgrounds and man-made electromagnetic interferences. The most direct method is a field test in a real environment, which, however, is expensive, time-consuming, and labor-intensive. Moreover, the field test may be uncontrollable and unrepeatable because of the rapid environmental changes. It would be difficult to locate and correct the errors in the development stage if the system failed in the field test. Therefore, the hardware-in-the-loop simulation method was proposed, which could verify the performance indicators in the infield and is the focus of this study. There are generally two infield test methods that target radar performance. One is the radio frequency (RF) injection method, in which the electromagnetic signals generated by the radar target simulator are fed into the RF receiver of the radar through the RF cable [10], [11]. The other is the RF radiation method based

The associate editor coordinating the review of this manuscript and approving it for publication was Amjad Gawanmeh.

on a triad array; it simulates the angular position of the target through the space vector synthesis of the three antennas [12], [13]. Therefore, the electromagnetic signals generated by the radar target simulator are spatially fed and transmitted toward the radar by the synthesized angular position. Three signals, namely the sum, difference, and another difference, need to be generated during the test process and injected into the three channels of the radar for the first method. The physical connections are more complex if a subarray-level phased array radar is involved, it may require connecting dozens of RF cables and are prone to error. Besides, this test system cannot produce electromagnetic radiation environments and can only be used to verify the back end rather than the whole radar. The second method, common in hardware-in-the-loop simulation, has been used since the 1960s and requires testing in an anechoic chamber [13]. The simulator generates the required target, environment, and interference signals, which are then radiated into the anechoic chamber. However, this method has four disadvantages. First, the system heavily relies on the RF channel composed of microwave devices. The complexity of signals in the space required for phased array radar verification determines the number of RF channels; thus, microwave devices' large-scale use is necessary, contrary to the trend of our digital era. Second, the large variations of the synthetic angle on the spherical array depend on the RF switching device, which has a response time that cannot match the fast beam scanning of the phased array. Third, spatial triad synthesis cannot simulate the spatial distribution characteristics of targets, and hence it is not suitable for simulating echo signals of the imaging radar, especially for the forward-looking ones. Fourth, this method belongs to a far-field test in which the construction conditions of the anechoic chamber are very strict, making the laboratory requirements expensive (which also restricts the subsequent development of joint test technology with multiple anechoic chambers).

In [14]–[18], the multi-probe radiation method is adopted to construct a ring layout near-field test environment, which can effectively test the frequency equipment performance of omnidirectional reception but was unsuitable for radar with strong antenna directivity. A fan-shaped multi-probe configuration method was proposed in [19] and [20], which could be applied to the radar detection process. However, they focused on the communication capacity but did not mention the angular position of the radar echo signal. Therefore, this study proposed a novel middle-field (between the near-field and far-field) test method based on multi-probe radiation. After the design of the test distance, probe layout (quantity and spacing), and the anechoic chamber size, the multi-channel baseband signals having adjustable amplitude and phase generated by the simulator were directly fed into the probe end via the microwave cable after upconversion and power control by the RF link. At the same time, the least square inversion method is used to solve the complex weight value of the probe so as to reconstruct the radiation and scattering characteristics of radar electromagnetic waves in the real environment, thereby realizing the simulation of the radar apparent center. By increasing the number of radiation channels and reducing the use of analog components, the new method can more realistically simulate a complex electromagnetic environment to test the whole radar system (including the antenna) compared to the injection simulation. Moreover, the study not only solves the severe requirement of the triad array method for far-field conditions but also adapts the beam agility of phased array by digitizing, which could be effectively used for evaluating the performance of phased array radar.

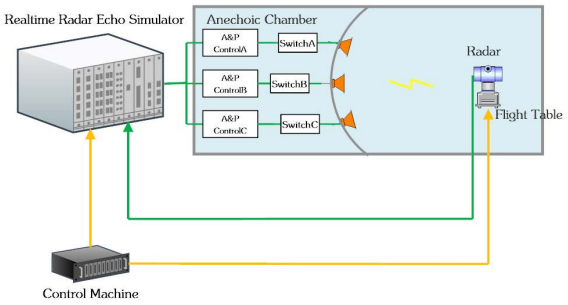

FIGURE 1. Typical setup of a radar performance evaluation system.

II. METHOD

A. SETUP OF TEST FACILITY

The general setup of a radar performance evaluation system is illustrated in Fig. 1. The probe is located on one side of the anechoic chamber on the glass fiber reinforced plastics or the steel cast spherical screen. The three-axis turntable used for attitude simulation is present in the quiet zone of the anechoic chamber, on which the testing equipment is installed. During the test, the spherical center of the screen, the gyration center of the turntable, and the phase center of the equipment antenna should coincide. The real-time radar echo simulator receives the control information from the simulation computer, generates the target echo signal, feeds it into the antenna through the RF link, and then radiates it towards the anechoic chamber through the antenna. In a conventional RF simulation system, three arbitrary antennas constituting an equilateral triangle on the spherical screen simultaneously radiate signals. When the baseband signal is generated, it is divided into three parts by the power divider, which then enter the three channels of the RF link. The feeding phases of the three channels remain the same, and the amplitudes determine the angular position of the synthetic signal. A configuration of the multi-probe radiation is considered in this paper. As shown in Fig. 2, the baseband generates multi-channel signals with adjustable amplitude and phase, which enter the spherical rectangular antenna array through microwave frequency conversion and power control. Therefore, plane wave conditions are formed in the test area, and the intersection between the inverse extension of the phase plane normal and the spherical surface of the antenna array

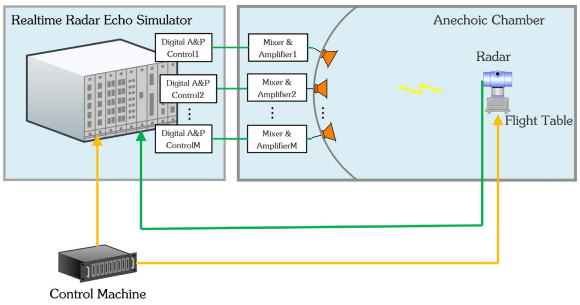

FIGURE 2. Multi-probe radiation setting in an anechoic chamber.

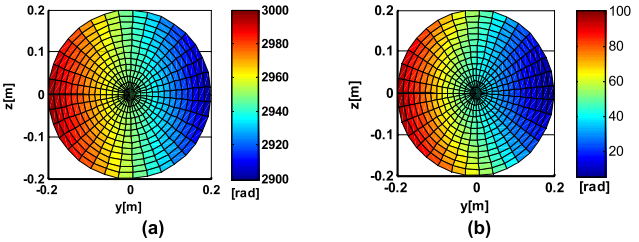

FIGURE 3. Phase distribution in the test area. (a) Large distance testing. (b) Small distance testing.

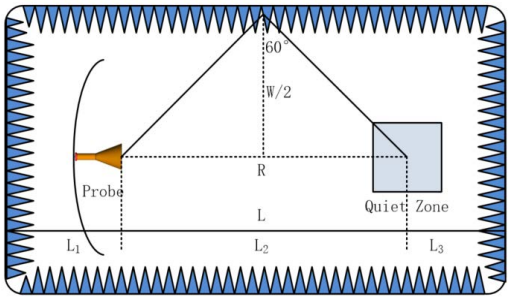

FIGURE 4. Cross-section of the designed anechoic chamber.

becomes the apparent center position synthesized by multiple probes.

The three key problems to be solved in multi-probe radiation simulation are as follows: First, under the selected test distance and anechoic chamber size, the radar antenna pattern should be consistent with the far-field pattern, and the performance of the test area of the anechoic chamber (quiet zone) should have a low reflectivity level (typically -45 dB to -50 dB in the Ku band). Second, an appropriate combination of the quantity feeding amplitude and phase control quantity (i.e., the complex weight matrix of the multi-probe antenna) is to be found so that the amplitude field distribution in the test area has maximum uniformity and the equiphase plane is close to the plane wave as much as possible. Third, the complex weight matrix should meet the simulation requirement of the apparent center position of the radar.

We can realize the multi-probe radiation simulation in the middle field of an anechoic chamber by solving the above problems.

B. ANECHOIC CHAMBER DESIGN

The distance between the radiation probe and the test area could affect the field phase stability of the entire area. When the test distance is large, i.e., the probe is in the far-field region of the tested radar antenna, the equiphase plane of the radiated electromagnetic wave could be approximated as a plane wave, as displayed on the left side of Fig. 3. The horizontal and vertical axes are represented under the anechoic chamber coordinate system O-XYZ, where O is the center of the spherical antenna array, the Y-axis is perpendicular to the back wall of the anechoic chamber and points to the radiation probes, and the Z-axis is perpendicular to the Y-axis and points up. Further, X-axis, Y-axis, and Z-axis constitute the right-hand coordinate system. When the test distance is small, i.e., the probe is in the near-field, the equiphase plane of the radiated electromagnetic wave is considerably bent, as displayed on the right side of Fig. 3.

Typically, the conventional simulation system based on triad synthesis required the test distance to meet the far-field condition of the tested radar antenna. A simulation method of middle-field testing is adopted in this work, and the test distance satisfies:

$$\frac{2d^2}{\lambda} < R < \frac{2D^2}{\lambda} \tag{1}$$

where R is the distance from the antenna phase center to the probe (radius of the sphere where the probe is located), d is the maximum size of the probe, D is the maximum size of the antenna for the tested radar, and λ is the working wavelength of the tested radar.

1) RADAR ANTENNA PATTERN

The test distance satisfies the formula above, i.e., the probe is in the Fresnel region of the radar antenna under test. The receiving pattern of the antenna will degenerate into a near-field distribution when the test distance is further reduced and the probe is in the reactive near-field of the antenna. Thus, there will be no null depth of the difference pattern (generally, a good directional sensitivity is present at 30 dB), and the antenna loses its direction-finding capability. Therefore, the place close to the Fraunhofer region in the Fresnel region must be selected to ensure consistent shapes of the antenna pattern and the far-field pattern. In other words, R should be close to $2D^2/\lambda$.

2) SIZE OF ANECHOIC CHAMBER

The size of the anechoic chamber can be designed after selecting the appropriate test distance. As displayed in Fig. 4, the length of the chamber is:

$$L = L_1 + L_2 + L_3 = L_1 + R + L_3 \tag{2}$$

where L_1 is the distance from the spherical screen to the front wall of the anechoic chamber, and L_1 is the distance

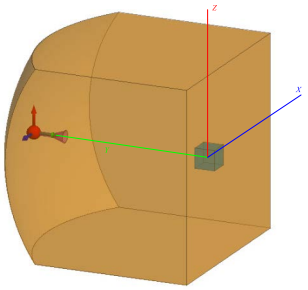

FIGURE 5. Quiet zone level calculation diagram (the left horn antenna was used as the radiation source in the chamber, and the blue cube area on the right was taken as the quiet zone of the chamber).

from the center of the quiet zone to the rear wall of the anechoic chamber. L_1 and L_2 generally take a quarter of the test distance R.

Generally, when the incident angle of the absorbing material is not greater than 60°, it can ensure that its reflectivity level meets the requirements, i.e., the width of the anechoic chamber satisfies [21]:

$$W > R\cot 60^\circ \tag{3}$$

The height and width of the anechoic chamber are generally similar to ensure that the reflection levels of different chamber surfaces are similar, that is, $H = W$.

3) REFLECTIVITY LEVEL OF QUIET ZONE

The next step involves determining the quiet zone performance of the designed anechoic chamber. To absorb the radio waves emitted by the radiation source, the inner wall of the chamber is pasted with wave-absorbing materials. Therefore, a low-echo area, named the quiet zone, is formed in the chamber. The reflectivity level of the quiet zone is defined by [22]:

$$\tau = \frac{E_r}{E_d} \tag{4}$$

where E_d is the direct wave from the radiation source to the quiet zone, and E_i is the reflected wave from the radiation source to the quiet zone. The reflections from the anechoic chamber's top, bottom, and four walls must all be considered. Therefore, the total reflected field intensity level is calculated as:

$$E_r = \left[\sum_{i=1}^{6} E_i^2\right]^{\frac{1}{2}} \tag{5}$$

where E_i represents the reflectivity level of the upper and lower, left and right, front and rear walls.

A high-precision quiet zone calculation method based on double-layer coatings, which could realize effective approximate high-frequency calculation for electrically super-large cavities, is described in Ref. [23]. As displayed in Fig. 5, a horn antenna was used as the radiation source to calculate the quiet zone reflectivity level of the anechoic chamber.

4) NUMBER OF PROBES

Two limitations exist while determining the number of probes required for multi-probe radiation:

(1) The maximum size of the multi-probe array should not exceed the beamwidth of the radar antenna under test. Generally, the beam width is small in the guidance radar frequency band; thus, the spherical array within the beam range can be regarded as a plane, implying that it satisfies:

$$\Delta d < \frac{R\theta_{BW} - d}{N - 1} \tag{6}$$

where N is the number of probes per row of the rectangular array; Δd is the spacing between probes; θ_{BV} is the beamwidth of the radar antenna under test (also known as the angular resolution).

The electromagnetic wave signal transmitted by the multiple probes cannot be vector synthesized at the antenna aperture if the formula above is not satisfied, which makes simultaneous radiation of the multiple probes pointless.

(2) The spacing of the probes is closely related to the size of the horn antenna (generally 8 cm in the Ku band), which can be described as:

$$\Delta d > d \tag{7}$$

In other words, when the horn antenna has a large size, the probe spacing must also be large (otherwise, there would be interference during installation).

Therefore, when the beamwidth of the antenna is fixed, the larger the array spacing, the fewer the probes would be in the spherical array. A larger beamwidth will correspond to more probes in the spherical array if the antenna spacing is fixed instead.

C. SIGNAL MODEL OF MULTI-PROBE

The modeling and simulation method of signals in the test area is briefly introduced for the scenario of multi-probe radiation in this section. The main contribution is by investigating the amplitude and phase distributions of the electromagnetic field in the anechoic chamber when multiple probes radiate simultaneously.

It is assumed that there are M probes in the spherical rectangular array. The plane of the antenna aperture field, which is located in the XOZ plane of the anechoic chamber coordinate system when the antenna is in the initial position, is taken as the test area, as displayed in Fig. 6.

And the test area covers only the antenna aperture, where there are P sampling points in total. Since the test area is located in the far-field region of the probe, the probe can be approximated as a point-source, and the propagation coefficient from the m ($m = 1, 2, \cdots, M$)th probe to the p ($p = 1, 2, \cdots, P$)th sampling point can be calculated as follows:

$$\alpha_{m,p} = \frac{\lambda}{4\pi d_{m,p}} e^{-j\frac{2\pi}{\lambda} d_{m,p}} \tag{8}$$

where $d_{m,p}$ represents the distance between the mth probe and the pth sampling point; λ is the radar signal wavelength.

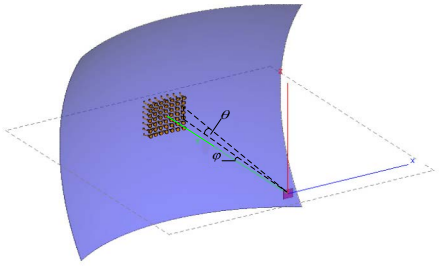

FIGURE 6. Spherical rectangular probe array. The blue part is the spherical screen used for installing the probes, and the purple part is the test area for placing the tested radar. φ and θ represent the pitch and azimuth angles at the apparent center.

The signal received at the pth sampling point can be calculated as the sum of the coherence of the signals transmitted by the probes as shown as follows:

$$R_p(t) = \sum_{m=1}^{M} \alpha_{m,p} S_m(t) \tag{9}$$

where $S_m(t)$ is the radiation signal at the aperture of the mth probe, which can be calculated as:

$$S_m(t) = E_m e^{-j2\pi ft+\phi_m} F\left(\theta_{m,p}\right) \tag{10}$$

where E_m is the feeding amplitude of the mth probe, which can be determined by the optimization algorithm; ϕ_m is the feeding phase of the radiation signal from the mth probe; $F(.)$ is the antenna pattern; $\theta_{m,p}$ is the off-axis angle between the line connecting the mth probe, the pth sampling point, and the pattern normal; f is the radar signal frequency.

Thus, the signal received at the pth sampling point in the test area can be calculated as:

$$R_p(t) = \sum_{m=1}^{M} \frac{\lambda}{4\pi d_{m,p}} e^{-j\frac{2\pi}{\lambda}d_{m,p}} E_m e^{-j(2\pi ft+\phi_m)} F\left(\theta_{m,p}\right) \tag{11}$$

According to the time-harmonic field theory, the time factor of Eq. (11) can be eliminated. p is an arbitrary sampling point in the test area, and the amplitude and phase-field distribution of the test area can be expressed by:

$$R_p = \sum_{m=1}^{M} \frac{\lambda}{4\pi d_{m,p}} e^{-j\frac{2\pi}{\lambda}d_{m,p}} E_m e^{j\phi_m} F\left(\theta_{m,p}\right) \tag{12}$$

We can attain two very important indexes of the anechoic chamber simulation by taking the modulus and phase of the above formula, respectively, namely phase uniformity and amplitude uniformity, which need to be optimized.

D. APPARENT CENTER

The core element in the simulation, which refers to the angular position of the signal synthesized by the probe array from the perspective of the radar, is the position of the apparent center. It physically means the line-of-sight position of the target when the radar is functioning.

The apparent center forms the intersection between the inverse extension of the normal of the equiphase plane of the synthetic array field and the array sphere from the perspective of the electromagnetic field. Therefore, we can solve the position of the apparent center if we could calculate the direction for the Poynting vector of the synthetic array field, i.e., the electromagnetic wave propagation direction of the synthetic field. Conversely, simulating a certain missile-target line-of-sight angle solves the corresponding apparent center position, which implies solving the multi-probe feeding amplitude and phase (these are the two control factors for the feeder control system of the array).

The calculation of the Poynting vector is too complex in practical engineering applications. Boeing initially proposed the amplitude gravity center formula method in the 1970s for a conventional triad. On the premise of ensuring the feeding phase balance for the three probes, the feeding amplitudes satisfy:

$$\begin{bmatrix} \varphi_1 & \varphi_2 & \varphi_3 \\ \theta_1 & \theta_2 & \theta_3 \\ 1 & 1 & 1 \end{bmatrix} \begin{bmatrix} E_1 \\ E_2 \\ E_3 \end{bmatrix} = \begin{bmatrix} \varphi \\ \theta \\ 1 \end{bmatrix} \tag{13}$$

where (φ_1, θ_i), $i = 1, 2, 3$ are the azimuth and pitch angles for the three probes in the polar coordinate system and (φ, θ) represent the pitch and azimuth angles at the apparent center.

The feeding amplitudes of the three probes can be obtained by inversing the matrix in Eq. (13), which is:

$$\begin{bmatrix} E_1 \\ E_2 \\ E_3 \end{bmatrix} = \begin{bmatrix} \varphi_1 & \varphi_2 & \varphi_3 \\ \theta_1 & \theta_2 & \theta_3 \\ 1 & 1 & 1 \end{bmatrix}^{-1} \begin{bmatrix} \varphi \\ \theta \\ 1 \end{bmatrix} \tag{14}$$

If the above method is adopted for the multi-probe radiation problem, the number of equations in the multivariate linear equation set to be solved would be less than the number of unknowns since the amplitudes and phases of the probes are controllable parameters. Therefore, the solution of the equation set is not unique, making it complex to obtain the amplitudes and phases of the probe directly. A new solution is proposed in this paper, which makes use of least-squares optimization to describe the probe amplitude and phase problem. In other words, a set of complex weights composed of amplitudes and phases should be sought such that the synthetic field radiated by the probes approaches the synthetic field of a conventional triad antenna.

According to Eq. (12), the following function model could be established for the multi-probe radiation field:

$$R_p = \mathbf{W}^H \mathbf{V}_p(x, z) \tag{15}$$

where $\mathbf{W}$ is the complex weight vector to be solved, $\mathbf{W} = \left[E_1 e^{j\phi_1}, E_2 e^{j\phi_2}, \mathrm{L}, E_M e^{j\phi_M}\right]^T$, and the superscript H represents the conjugate transposition; $\mathbf{V}_p(x, z)$ is the propagation vector from the probe to the sampling point in the test area:

$$\mathbf{V}_p(x, z) = \left[\frac{\lambda}{4\pi d_{1,p}} e^{-j\frac{2\pi}{\lambda}d_{1,p}} F\left(\theta_{1,p}\right), \frac{\lambda}{4\pi d_{2,p}} e^{-j\frac{2\pi}{\lambda}d_{2,p}}\right.$$

$$\times F\left(\theta_{2,p}\right), \cdots, \frac{\lambda}{4\pi d_{M,p}} e^{-j\frac{2\pi}{\lambda}d_{M,p}} F\left(\theta_{M,p}\right)\Big]^T \tag{16}$$

Assuming that R_{p0} is the synthetic target field distribution at the sampling point p in the test area, then the least square error is defined as:

$$\xi = \iint_D \left|R_{p0} - R_p\right|^2 dxdz = \iint_D \left|R_{p0} - \mathbf{W}^H \mathbf{V}_p\left(x, z\right)\right|^2 dxdz \tag{17}$$

where D is the test area in the XOZ plane.

The complex gradient of $\mathbf{W}^H$ is obtained by using the above error function and is assigned with a value of zero, i.e.,

$$\iint_D \mathbf{V}_p\left(x, z\right) R_{p0}^* dxdz - \left[\iint_D \mathbf{V}_p\left(x, z\right) \mathbf{V}_p^H\left(x, z\right) dxdz\right] \mathbf{W} = 0 \tag{18}$$

where the superscript * represents conjugation. Let the cross-covariance matrix between the propagation vector and the synthetic target field be:

$$\mathbf{R}_{VR} = \iint_D \mathbf{V}_p\left(x, z\right) R_{p0}^* dxdz \tag{19}$$

Let the auto-covariance matrix of the propagation vector be:

$$\mathbf{R}_{VV} = \iint_D \mathbf{V}_p\left(x, z\right) \mathbf{V}_p^H\left(x, z\right) dxdz \tag{20}$$

Then, Eq. (18) can be simplified as follows:

$$\mathbf{W} = \mathbf{R}_{VV}^{-1} \mathbf{R}_{VR} \tag{21}$$

This formula describes the optimal value of the complex weight matrix of the multi-probe antenna under the least-squares criterion.

III. SIMULATION RESULT

A. TEST DISTANCE

In this study, two types of antennas were selected to analyze the influence of the test distance on the antenna radiation field distribution.

(1) Pyramidal horn antenna. The operating frequency was set to 1.645 GHz, and the dimensions for the aperture size of the antenna were 550 mm×428 mm. The test distance was scanned from 0.6 m to 3.6 m, and the E-plane and H-plane amplitude distribution curves of the antenna radiation field were calculated, respectively, and the results are shown in Fig. 7.

The far-field condition (boundary condition of near-field and far-field radiation regions) of the pyramid horn antenna was calculated to be 3.3 m, according to Eq. (1). The angular

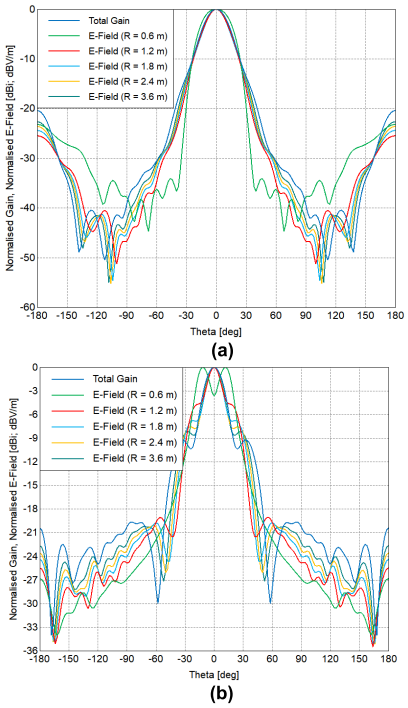

FIGURE 7. Antenna patterns of the pyramidal horn antenna. (a) Antenna pattern of E-plane. (b) Antenna pattern of H-plane.

power distribution of the radiation field should be maintained consistently when the test distance exceeds this threshold. The reactive near-field region (within 3–5 wavelengths) belonged to the electromagnetic oscillation area in which the radiation field distribution had poor directivity (the E-plane curve became gentler, and the H-plane curve exhibited beam splitting). The field directivity improved in the near-field radiation area. The radiation field distributions were the same in the main lobe and the first side lobe when the test distance exceeded 1.8 m (half of the boundary condition).

(2) Waveguide slot array antenna. The working frequency was set as 10 GHz, the maximum aperture size of the antenna was 151 mm, and the test distance ranged from 0.15 m to 2.4 m. Fig. 8 shows the calculated E-plane and H-plane amplitude distribution curves of the antenna radiation field.

Similarly, the far-field condition of the waveguide slot array antenna was calculated to be 1.5 m by using Eq. (1). The angular power distribution of the radiation field should be consistent when the test distance exceeds this threshold. The reactive near-field region belonged to the electromagnetic oscillation area; thus, the directionality of the radiation field distribution was similarly poor. The directionality of the radiation field improved gradually in the near-field radiation area. When the test distance exceeded 0.6 m (0.4 times the boundary condition), the radiation field distributions remained the same in the main lobe and the first side lobe.

Therefore, when the test distance was half of the far-field condition in the Fresnel region of the antenna, we could ensure that the radiation field distribution of the antenna near

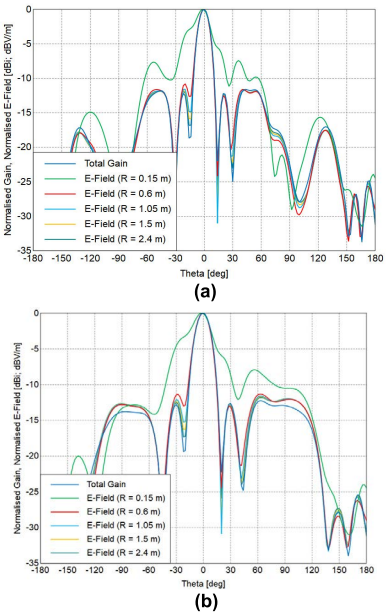

FIGURE 8. Antenna patterns of the waveguide slot array antenna. (a) Antenna pattern of E-plane. (b) Antenna pattern of H-plane.

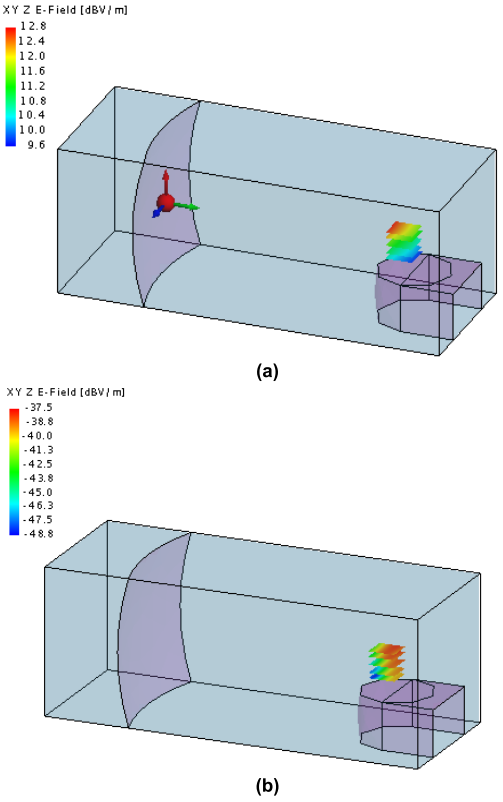

FIGURE 9. Radiation field in the quiet zone of the anechoic chamber (a) Radiation field and scattering field. (b) Only scattering field.

the main lobe was similar to that of the far-field. 0.6 times of the far-field condition was taken as the test distance to maintain some error margin.

B. REFLECTIVITY LEVEL

In this work, the working frequency of the tested radar was 15 GHz, and the aperture size was 400 mm×400 mm; hence the calculated far-field condition was 16 m. Here, the test distance of the anechoic chamber was selected to be 9.6 m (0.6 times the boundary distance).

As calculated by Eq. (2), the length of the anechoic chamber was $9.6 + 2.4 + 2.4 + 14.4m$, and the width of the anechoic chamber was $9.6\cot 60 = 5.54m$ as calculated by Eq. (3). The width and height were both 5.54 m; therefore, the size of the anechoic chamber had the dimensions of 14.4 m (length)×5.54 m (width)×5.54 m (height).

The PO-GO joint algorithm was used for simulating the quiet zone performance of the anechoic chamber based on the modeling theory of a metal shell coated with a double-layer medium, as described in Ref. [23]. The quiet zone had the dimensions of 1 m (length)×1 m (width)×1 m (height). The calculation results are displayed in Fig. 9.

The combined field distribution of the incident field and the reflected field in the quiet zone are shown on the left side of Fig. 9. The maximum level was at the top of the quiet zone near the radiation source due to the influence of the test bench, and the figure on the right illustrates the reflected field distribution in the quiet zone. The reflection of the rear wall had a great impact on the quiet zone, and the maximum level was seen at the side near the rear wall. The interpolation of the two calculation results could be regarded as the reflected level of the quiet zone since the incident field was much larger than the reflected field. As shown in the figure, the quiet zone level of the chamber was less than −50 dB when the working frequency was 15 GHz, thus, meeting the design requirements. Therefore, the test distance of 9.6 m could be used in subsequent calculations.

TABLE 1. Relationship between the triad's apparent center and the feeding amplitude.

φ (mrad)	θ (mrad)	E1 (V)	E2 (V)	E3 (V)
0	0	1/3	1/3	1/3
0	7.3	0.25	0.25	0.5
−7.3	7.3	0.4167	0.0833	0.5
7.3	−7.3	0.25	0.5833	0.1667

C. SOLUTION FOR COMPLEX WEIGHTS

Solving the complex weights of the probes is practiced to calculate their feeding amplitudes and phases.

Initially, the conventional triad mode was discussed. According to the amplitude gravity center formula, the amplitude feeding control was performed for the three probes. Table 1 displays the required triad amplitudes during different apparent center positions.

Fig. 10 shows the synthetic amplitude and phase fields of the triads during different apparent center positions. At most testing positions of the antenna aperture, the phase difference was within 10 degrees when different apparent center

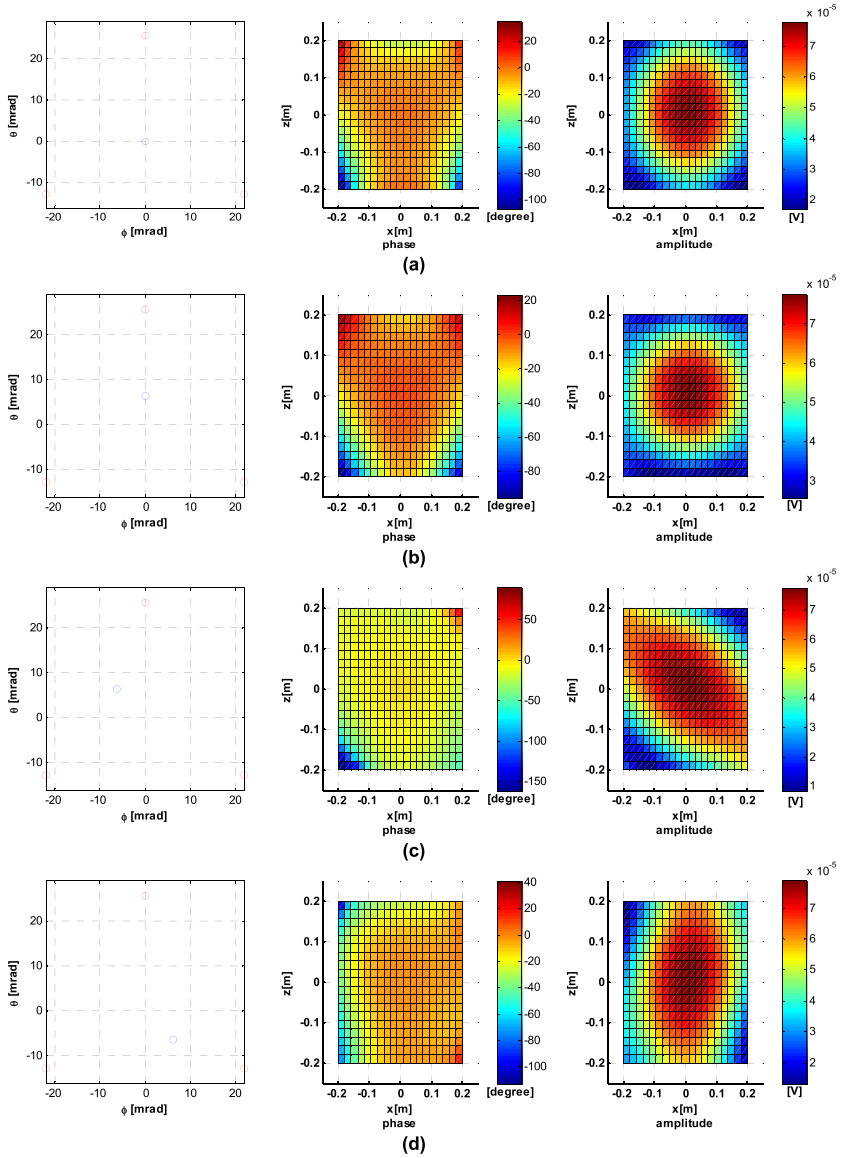

FIGURE 10. **Synthetic field amplitude and phase distributions during various apparent center positions (the red circles in the first column indicate the antenna position, and the blue circles indicate the apparent center position) when the test distance was 20 m (in the far-field region of the antenna). (a) $\varphi = 0, \theta = 0$. (b) $\varphi = 0, \theta = 7.3$. (c) $\varphi = -7.3, \theta = 7.3$. (d) $\varphi = 7.3, \theta = -7.3$.**

positions were synthesized by the triad through amplitude feeding changes. The phase wavefront was approximately planar, and the amplitude uniformity was less than 2 dB.

The number of probes and their spacing in the array are discussed below. The beamwidth of a typical guidance radar antenna was selected by taking the apparent center angle (7.3, −7.3) as an example. In Fig. 11, the amplitude and phase distributions of the multi-probe radiation field after complex weighting through least-squares optimization are given, where the number of array elements was varied.

As seen from Fig. 11, when the number of array elements exceeded 5×5, the least square error became very small, and the amplitude and phase distributions remained consistent with those shown in the subfigures above. The influence of the test distance and the probe number on the least square error were further considered.

Various test distances and probe numbers were selected, and in Table 2, the spacings of the rectangular antenna arrays were displayed in which the values that met the requirements were marked gray.

The root mean squares of the amplitude and the phase errors were calculated on the premise that the spacing met the requirements. From Fig. 12, it could be seen that the following laws were satisfied at various test distances. The appropriate complex weight could not be found when the number of array elements was 2×2, which was equivalent to the synthetic field of a triad. When the number of elements was

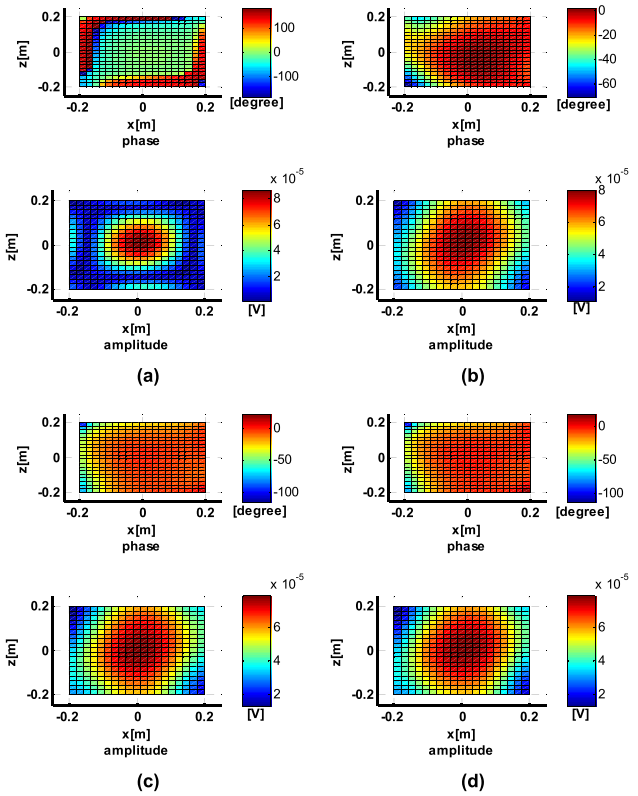

FIGURE 11. Distributions of the synthetic radar aperture field corresponding to various array elements. (a) 2 × 2. (b) 3 × 3. (c) 5 × 5. (d) 7 × 7.

TABLE 2. Antenna spacings corresponding to various array elements.

	M=4 (2×2)	M=9 (3×3)	M=16 (4×4)	M=25 (5×5)	M=49 (7×7)
5 m	0.24	0.12	0.08	0.06	0.04
8 m	0.43	0.21	0.14	0.10	0.07
9.6 m	0.53	0.26	0.17	0.13	0.088
16 m	0.93	0.46	0.31	0.23	0.155

3 × 3, the magnitude of the least square error was reduced by two orders after complex weighting, the amplitude error could meet the requirement, but the phase error was still large. The root-mean-square of the amplitude in the least square error was less than 0.05 dB after complex weighting when the number of array elements was greater than 5 × 5, and the root-mean-square of the phase was less than 2°; thus, its influence on the synthetic field distribution and apparent center position could be ignored. Therefore, the number of the multi-probe radiation array units was selected as 5 × 5 for the simulation of the apparent center.

The feeding amplitude and phase values of the probes were solved by using the least-squares method by simultaneously radiating a 5 × 5 rectangular array, and the results are displayed in Tables 3 and 4. The apparent center could be altered to evaluate the radar performance through attenuation and phase shift modulation of the baseband signal.

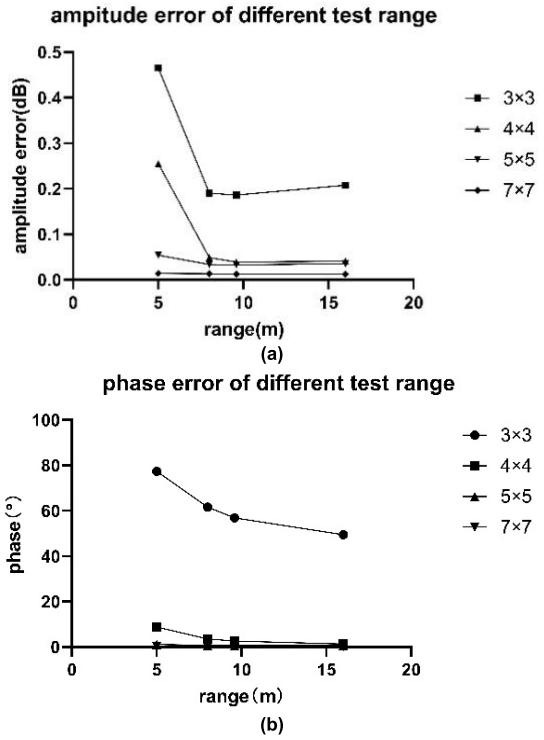

FIGURE 12. Least square errors corresponding to a variety of units and test distances. (a) Amplitude error. (b) Phase error.

TABLE 3. Normalized feeding amplitudes.

Unit: V

	1	2	3	4	5
1	0.013	0.072	0.090	0.138	0.039
2	0.117	0.382	0.506	0.610	0.201
3	0.207	0.579	1.000	0.683	0.298
4	0.131	0.455	0.721	0.621	0.230
5	0.027	0.137	0.291	0.217	0.072

TABLE 4. Feeding phases.

Unit: Degree

	1	2	3	4	5
1	164.783	-111.272	48.443	-125.236	65.357
2	-66.778	61.313	-131.296	36.111	-123.155
3	29.330	-157.604	9.120	-178.641	17.645
4	-120.468	36.750	-161.123	12.158	-149.549
5	72.896	-109.497	36.389	-139.553	48.351

IV. CONCLUSION

This paper discussed the feasibility of the radar performance evaluation based on conducting multi-probe radiation in an anechoic chamber. New requirements for evaluating the phased array radar were determined and discussed when compared to conventional mechanical array radar testing. A few key aspects of the multi-probe radiation design for

the phased array radar, such as the effective test distance, size of the anechoic chamber, number of probe antennas, and feeding amplitudes and phases of the probes, were studied. The simulation results revealed that when the radar operating frequency was 15 GHz and the antenna aperture was 400 mm×400 mm, 9.6 m was an optional test distance, which was located in the Fresnel region of the radar antenna under test. The quiet zone level was less than −50 dB, meeting the applicational requirements of radar performance evaluation. The proposed multi-probe simultaneous radiation method could be used to fit the synthetic field of a conventional triad. A rectangular array with 5 × 5 probes and a spacing of 13 cm was selected when the half-power beamwidth of the antenna was 4°. By weighting the probe feeding amplitude and phase, the root-mean-square of the least square error of the synthetic field amplitude was found to be 0.0327 dB, and the root mean square error of the phase was 0.6492°, indicating that the accuracy of the apparent center position from the multi-probe radiation synthesis could also meet the requirements of radar performance evaluation. A small anechoic chamber for testing was realized through the design and configuration of the multi-probe radiation anechoic chamber, which effectively reduced the system construction cost. Furthermore, a more complex electromagnetic environment was established, which was more suitable for the phased array radars. This constituted an update for the existing anechoic chamber system.

Future works on this topic include:

1) Amplitude and phase consistency between multiple channels after calibration. Inconsistency in the amplitude and phase could affect the simulation accuracy of the apparent center position, which would require further investigation.

2) The follow-up study will consider the influence of polarization characteristics.

REFERENCES

[1] W. Montlouis, R. Fauconier, and M. Ndoye, "Rapidly moving target parameter estimation using phased array radars," in *Proc. 43rd Int. Conf. Telecommun. Signal Process. (TSP)*, Milan, Italy, Jul. 2020, pp. 523–527.

[2] O. Kechagias-Stamatis, N. Aouf, G. Gray, L. Chermak, M. Richardson, and F. Oudyi, "Local feature based automatic target recognition for future 3D active homing seeker missiles," *Aerosp. Sci. Technol.*, vol. 73, pp. 309–317, Feb. 2018.

[3] Q. Wen, T. Lu, Q. Xia, and Z. Sun, "Beam-pointing error compensation method of phased array radar seeker with phantom-bit technology," *Chin. J. Aeronaut.*, vol. 30, no. 3, pp. 1217–1230, 2017.

[4] C. H. Hwang, T. H. Joo, J. M. Park, K. Kim, and J. S. Jung, "Fast digital multi-beam search method for active phased array antenna system with full azimuth beam steering," *J. Electromagn. Waves Appl.*, vol. 36, no. 4, pp. 1–18, 2021, doi: 10.1080/09205071.2021.1977184.

[5] W. Huo, Q. Zhang, Y. Zhang, Y. Zhang, Y. Huang, and J. Yang, "A superfast super-resolution method for radar forward-looking imaging," *Sensors*, vol. 21, no. 3, p. 817, Jan. 2021, doi: 10.3390/s21030817.

[6] A. S. de Sena, "Massive MIMO-NOMA networks with imperfect SIC: Design and fairness enhancement," *IEEE Trans. Wireless Commun.*, vol. 19, no. 9, pp. 6100–6115, Jun. 2020.

[7] E. Kim, J. Kwak, and S. Chong, "Virtual beamforming and user scheduling for sub-array architecture in mmWave networks," *IEEE Commun. Lett.*, vol. 23, no. 1, pp. 168–171, Jan. 2019.

[8] Z. Xie, J. Zhu, C. Fan, and X. Huang, "An improved sub-array adaptive beamforming technique based on multiple sources of errors," *J. Mar. Sci. Eng.*, vol. 8, no. 10, p. 757, Sep. 2020, doi: 10.3390/jmse8100757.

[9] G. Babur, G. O. Manokhin, A. A. Geltser, and A. A. Shibelgut, "Low-cost digital beamforming on receive in phased array radar," *IEEE Trans. Aerosp. Electron. Syst.*, vol. 53, no. 3, pp. 1355–1364, Jun. 2017.

[10] S. Piyaratna, N. Duong, J. Carr, D. Bird, S. Kennedy, A. Udina, and P. Jenkinson, "Digital RF processing system for Hardware-in-the-Loop simulation," in *Proc. Int. Conf. Radar*, Adelaide, SA, Australia, Sep. 2013, pp. 554–559.

[11] Y. Yiwei, S. Jie, and X. Wei, "Design and implementation of a Hardware-in-the-loop radar simulation test system," in *Proc. IEEE 2nd Int. Conf. Inf. Commun. Signal Process. (ICICSP)*, Weihai, China, Sep. 2019, pp. 161–164.

[12] X. Liu, J. Liu, F. Zhao, X. Ai, and G. Wang, "An equivalent simulation method for pulse radar measurement in anechoic chamber," *IEEE Geosci. Remote Sens. Lett.*, vol. 14, no. 7, pp. 1081–1085, Jul. 2017.

[13] M. Pywell and M. Midgley-Davies, "Aircraft-sized anechoic chambers for electronic warfare, radar and other electromagnetic engineering evaluation," *Aeronaut. J.*, vol. 121, no. 1244, pp. 1393–1443, Oct. 2017.

[14] Y. Miao, W. Fan, J. Takada, R. He, X. Yin, M. Yang, J. Rodríguez-Piñeiro, A. A. Glazunov, W. Wang, and Y. Gong, "Comparing channel emulation algorithms by using plane waves and spherical vector waves in multiprobe anechoic chamber setups," *IEEE Trans. Antennas Propag.*, vol. 67, no. 6, pp. 4091–4103, Jun. 2019.

[15] Y. Li, L. Xin, X. Liu, and X. Zhang, "Dual anechoic chamber setup for over-the-air radiated testing of 5G devices," *IEEE Trans. Antennas Propag.*, vol. 68, no. 3, pp. 2469–2474, Mar. 2020.

[16] W. Fan, X. C. B. de Lisbona, F. Sun, J. O. Nielsen, M. B. Knudsen, and G. F. Pedersen, "Emulating spatial characteristics of MIMO channels for OTA testing," *IEEE Trans. Antennas Propag.*, vol. 61, no. 8, pp. 4306–4314, Aug. 2013.

[17] A. Khatun, V.-M. Kolmonen, V. Hovinen, D. Parveg, M. Berg, K. Haneda, K. I. Nikoskinen, and E. T. Salonen, "Experimental verification of a plane-wave field synthesis technique for MIMO OTA antenna testing," *IEEE Trans. Antennas Propag.*, vol. 64, no. 7, pp. 3141–3150, Jul. 2016.

[18] Y. L. Ji, W. Fan, G. F. Pedersen, and X. F. Wu, "On channel emulation methods in multiprobe anechoic chamber setups for over-the-air testing," *IEEE Trans. Veh. Technol.*, vol. 67, no. 8, pp. 6740–6751, Apr. 2018.

[19] P. Kyösti, L. Hentilä, W. Fan, J. Lehtomäki, and M. Latva-Aho, "On radiated performance evaluation of massive MIMO devices in multiprobe anechoic chamber OTA setups," *IEEE Trans. Antennas Propag.*, vol. 66, no. 10, pp. 5485–5497, Oct. 2018.

[20] W. Fan, I. Carton, P. Kyosti, A. Karstensen, T. Jamsa, M. Gustafsson, and G. F. Pedersen, "A step toward 5G in 2020: Low-cost OTA performance evaluation of massive MIMO base stations," *IEEE Antennas Propag. Mag.*, vol. 59, no. 1, pp. 38–47, Feb. 2017.

[21] I. Exposito, M. G. Sanchez, and I. Cuinas, "Uncertainty assessment of a small rectangular anechoic chamber: From design to operation," *IEEE Trans. Antennas Propag.*, vol. 68, no. 6, pp. 4871–4880, Jun. 2020.

[22] D. A. Song, Q. Zhang, and H. M. Liao, "A beamwidth modified model for calculation of reflected level of quiet zone in anechoic chamber," in *Proc. Int. Appl. Comput. Electromag. Soc. Symp.*, Suzhou, China, Aug. 2017, pp. 1–4.

[23] R. X. Xu, P. Zhou, and J. W. Zhang, "Calculation method for quiet zone of anechoic chamber based on double layer coating model," *J. Huazhong Univ. Sci. Technol. Natural Sci. Ed.*, vol. 43, no. 11, pp. 73–77, Nov. 2015.

RUOXI XU was born in Hubei, China, in 1987. He received the B.S. degree from the Huazhong University of Science and Technology, Wuhan, China, in 2010, and the Ph.D. degree in navigation guidance and control from the Second Academy of China Aerospace, Beijing, China, in 2016.

In 2016, he joined the Beijing Institute of Control and Electronic Technology, where he is currently an Associate Professor. His current research interests include radio frequency system simulation, phased array radar test, and radar imaging algorithms.

XIAO HE received the B.S. degree from Tianjin University, Tianjin, China, in 2006, and the M.S. degree in electromagnetic field and microwave technology from the Second Academy of China Aerospace, Beijing, China, in 2009.

He is currently a Professor with the Beijing Institute of Control and Electronic Technology. His current research interests include radio frequency system simulation and electromagnetic calculation.

YUANYUAN YANG was born in Henan, China, 1992. He received the M.S. degree in electronic engineering from Nankai University, Tianjin, China, in 2014.

From 2014 to 2017, he was an Engineer engaging in designing anechoic chambers at China Aerospace Construction Group Company Ltd. Since 2018, he has been with the Beijing Institute of Control and Electronic Technology, where he is currently an Engineer in RF simulation. His current research interests include radar terminal guidance simulation and radar signal processing algorithms.

HONGDA YAO received the B.S. and M.S. degrees in electronic engineering from the University of Electronic Science and Technology of China (UESTC), Chengdu, China, in 2007.

He is currently a Professor with the Beijing Institute of Control and Electronic Technology. His current research interests include radar test and electromagnetic calculation.

QIAN WU received the B.S. and M.S. degrees in navigation guidance and control from Wuhan University, Wuhan, China, in 2013.

In 2016, she joined the Beijing Institute of Control Engineering, where she is currently an Associate Professor. Her current research interest includes computer software technology.